MNRAS 000, 1–8 (2016) Preprint 15 November 2016 Compiled using MNRAS LATEX style file v3.0

A minimal empirical model for the cosmic far-infrared background anisotropies

Hao-Yi Wu[1,2⋆] and Olivier Doré[1,2]
[1] California Institute of Technology, MC 367-17, Pasadena, CA 91125, USA
[2] Jet Propulsion Laboratory, 4800 Oak Grove Drive, Pasadena, CA 91109, USA

arXiv:1611.04517v1 [astro-ph.GA] 14 Nov 2016

15 November 2016

ABSTRACT

Cosmic far-infrared background (CFIRB) probes unresolved dusty star-forming galaxies across cosmic time and is complementary to ultraviolet/optical probes of galaxy evolution. In this work, we interpret the observed CFIRB anisotropies using an empirical model based on recent galaxy survey results, including stellar mass functions, star-forming main sequence, and dust attenuation. Without introducing new parameters, our model agrees well with the CFIRB anisotropies observed by *Planck* and the submillimeter number counts observed by *Herschel*. We find that the commonly used linear relation between infrared luminosity and star-formation rate over-produces the observed CFIRB amplitudes, and lower infrared luminosities from low-mass galaxies are required. Our results indicate that CFIRB not only provides a consistency check for galaxy evolution models but also informs the star-formation rate and dust content for low-mass galaxies.

Key words: galaxies: haloes — galaxies: star formation — submillimetre: diffuse background — submillimetre: galaxies

1 INTRODUCTION

Cosmic far-infrared background (CFIRB) originates from unresolved dusty star-forming galaxies from all redshifts and accounts for half of the extragalactic background light generated by galaxies. In dusty star-forming galaxies, $\sim 90\%$ of the ultraviolet (UV) photons produced by recent star-forming activities are absorbed by interstellar dust and re-emitted in far-infrared (FIR; also known as submillimeter, submm; 100–1000 μm). The FIR luminosities of galaxies are thus tracers of star-formation rate (SFR) and are complementary to UV luminosities (e.g., Kennicutt 1998; Kennicutt & Evans 2012; Madau & Dickinson 2014). Compared with UV, galaxies are much less understood in FIR/submm due to the low-resolution of telescopes in these wavelengths. Despite the recent progress in resolving galaxies in FIR/submm (e.g., Lutz 2014; Casey et al. 2014; Geach et al. 2016; Dunlop et al. 2016; Fujimoto et al. 2016), most of the dusty star-forming galaxies remain unresolved. Therefore, CFIRB provides a rare opportunity to study the dusty star-forming galaxies under the current resolution limit.

First predicted by Partridge & Peebles (1967), CFIRB was discovered by *COBE*-FIRAS, which also provided to date the only absolute intensity measurement of CFIRB (Puget et al. 1996; Fixsen et al. 1998; Hauser et al. 1998; Gispert et al. 2000; Hauser & Dwek 2001). Thereafter, the anisotropies of CFIRB have been measured to ever-improving accuracy by *Spitzer* (Lagache et al. 2007), BLAST (Viero et al. 2009), SPT (Hall et al. 2010), AKARI (Matsuura et al. 2011), ACT (Hajian et al. 2012), *Herschel*-SPIRE (Amblard et al. 2011; Berta et al. 2011; Viero et al. 2013), and *Planck*-HFI (Planck Collaboration XVIII 2011; Planck Collaboration XXX 2014). In addition, CFIRB maps have been cross-correlated with the lensing potential observed using cosmic microwave background (CMB, Planck Collaboration XVIII 2014) and with near-infrared background (Thacker et al. 2015).

The CFIRB anisotropies have been interpreted mostly using phenomenological models (e.g., Viero et al. 2009; Amblard et al. 2011; Planck Collaboration XVIII 2011; De Bernardis & Cooray 2012; Xia et al. 2012; Shang et al. 2012; Addison et al. 2013; Viero et al. 2013; Planck Collaboration XXX 2014). Although these models can fit the data, they provide limited insight into the underlying galaxy evolution processes. Since galaxy evolution has been extensively studied by UV/optical surveys, it is necessary to understand whether CFIRB agrees with the current knowledge of galaxy evolution.

In this work, we construct an empirical model for dusty star-forming galaxies based on recent galaxy survey re-

⋆ E-mail: hywu@caltech.edu

© 2016 The Authors

sults, including stellar mass functions, star-forming main sequence, and dust attenuation. We find that, without introducing new parameters, a minimal model can well reproduce the observed CFIRB anisotropies and submm number counts. Our model is the first step toward constructing a comprehensive model for UV, optical, and FIR observations, as well as building multi-wavelength mock catalogs for these observations. Such a model is essential for the understanding of cosmic star-formation history and for extracting the most information from multi-wavelength surveys.

Our approach is similar to the empirical approach adopted by Béthermin et al. (2012a,c, 2013). Our major innovations include using an N-body simulation and recent self-consistent compilations of stellar mass functions and star-forming main sequence. We also adopt a minimalist approach; that is, we look for the simplest, observationally-motivated model that agrees with CFIRB observations. In each step of our modeling, we directly use constraints from recent observations and avoid introducing new parameters or fitting model to the data. This work is complementary to our earlier work of interpreting CFIRB using a physical gas regulator model (Wu et al. 2016).

This paper is organized as follows. We introduce our model in Section 2 and calculate the CFIRB anisotropies in Section 3. Section 4 compares our model predictions with the observational results of *Planck* and *Herschel*. We discuss our results in Section 5 and summarize in Section 6. Throughout this work, we use the cosmological parameters adopted by the Bolshoi-Planck simulation (see Section 2.1), the stellar population synthesis (SPS) model from Bruzual & Charlot (2003, BC03), and the initial mass function (IMF) from Kroupa (2001).

2 EMPIRICAL MODEL

We construct a model to generate the infrared (IR) spectral flux densities S_ν for a population of galaxies. Our model includes five steps:

(i) Sampling dark matter haloes from the Bolshoi-Planck simulation (Section 2.1)
(ii) Performing abundance matching to assign stellar mass (M_*) to haloes (Section 2.2)
(iii) Assigning SFR to M_* based on the star-forming main sequence (Section 2.3)
(iv) Calculating IR luminosity ($L_{\rm IR}$) based on SFR and M_* (Section 2.4)
(v) Calculating S_ν by assuming a spectral energy distribution (SED; Section 2.5)

Steps (ii), (iii), (iv) are demonstrated in Figure 1. Below we describe each step in detail.

2.1 Dark matter haloes from the Bolshoi-Planck simulation

We use the public halo catalogs of the Bolshoi-Planck simulation (Rodríguez-Puebla et al. 2016)[1], which is based on a ΛCDM cosmology consistent with the *Planck* 2013 results (Planck Collaboration XVI 2014): $\Omega_\Lambda = 0.693$; $\Omega_M = 0.307$; $\Omega_b = 0.048$; $h = 0.678$; $n_s = 0.96$; $\sigma_8 = 0.823$. The simulation has a box size of 250 h^{-1}Mpc and a mass resolution of $1.5 \times 10^8 h^{-1}{\rm M}_\odot$.

The simulation is processed with the Rockstar halo finder (Behroozi et al. 2013a) and Consistent Trees (Behroozi et al. 2013b). Therefore, the halo catalogs include the mapping between central haloes and subhaloes, as well as the peak circular velocity of a halo in its history ($v_{\rm peak}$). In this work, we use all haloes with $v_{\rm peak} > 100$ km/s between $z = 0.25$ and $z = 5$, with a redshift interval of $\Delta z \approx 0.25$. When calculating theoretical uncertainties (see Section 4), we use 0.1% of the haloes in the simulation (∼6000 haloes in the $z = 0.25$ snapshot) to facilitate the calculation.

2.2 Stellar mass from abundance matching

To assign a stellar mass to each halo, we perform abundance matching between $v_{\rm peak}$ and observed stellar mass functions. The basic concept of abundance matching is to assign higher stellar masses to more massive haloes based on the number density, either monotonically or with some scatter (e.g., Vale & Ostriker 2004; Shankar et al. 2006; Behroozi et al. 2013c; Moster et al. 2013). Instead of halo mass, we use $v_{\rm peak}$, which is less affected by mass stripping and better correlated with stellar mass (e.g., Nagai & Kravtsov 2005; Conroy et al. 2006; Wang et al. 2006; Wetzel & White 2010; Reddick et al. 2013).

First, we collect observed stellar mass functions from the literature. For $z \leq 3$, we use the recent compilation of stellar mass functions by Henriques et al. (2015, see their Figures 2 and A1)[2], which are calibrated with the *Planck* cosmology. Following Henriques et al. (2015), we add $\Delta M_* = 0.14$ to convert to the BC03 SPS model. For $z \geq 4$, we use the stelar mass functions by Song et al. (2016, see their Table 2), which are derived from the rest-frame UV observations from CANDELS, GOODS, and HUDF, based on the BC03 SPS model.

Second, we fit the stellar mass functions using redshift-dependent Schechter functions (see Appendix A). For $0 \leq z \leq 3.5$, we use a double Schechter function with constant faint-end slopes; for $3.5 < z \leq 6$, we use a single Schechter function with a time-dependent slope. Using the fitting functions presented in Appendix A, we are able to interpolate smoothly between redshifts. The left panel of Figure 1 shows the data points and the fitting functions. Although we fit the stellar mass function out to $z = 6$, we only use galaxies at $z \leq 5$ in our calculations.

Third, we perform abundance matching between the stellar mass functions and the $v_{\rm peak}$ of haloes, assuming a scatter of 0.2 dex (e.g., Reddick et al. 2013). In the calculation, the input stellar mass function is first deconvolved with the scatter, and then the deconvolved stellar mass function is used to assign M_* to $v_{\rm peak}$ monotonically. We use the code provided by Y.-Y. Mao[3], which follows the implementation in Behroozi et al. (2010, 2013c). With this step, a stellar mass is assigned to each halo.

[1] http://hipacc.ucsc.edu/Bolshoi/MergerTrees.html

[2] The data sets are publicly available at http://galformod.mpa-garching.mpg.de/public/LGalaxies/figures_and_data.php.
[3] https://bitbucket.org/yymao/abundancematching

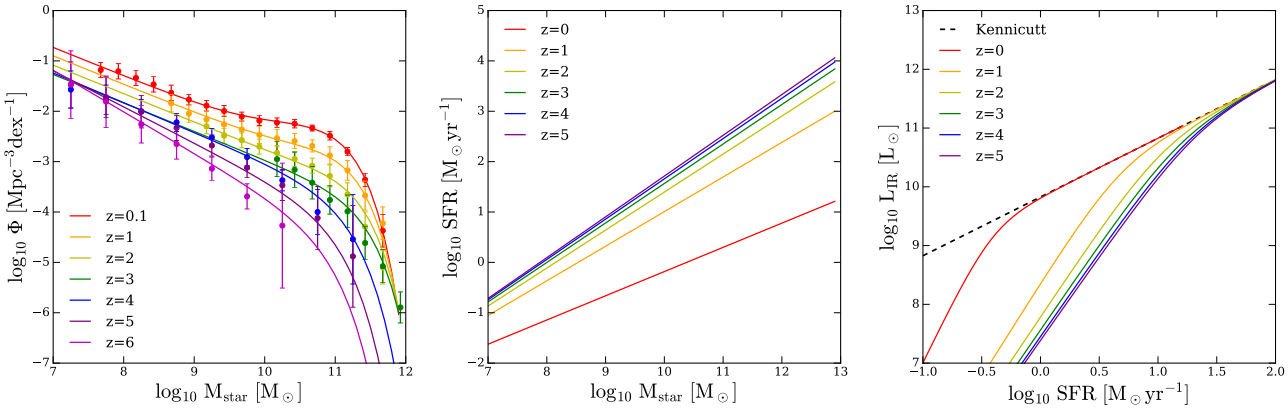

Figure 1. Key elements of our model. **Left**: Stellar mass functions from Henriques et al. (2015) and Song et al. (2016). We fit redshift-dependent Schechter functions to the data and preform abundance matching between M_* and $v_{\rm peak}$ (see Section 2.2 and Appendix A). **Center**: Star-forming main sequence from Speagle et al. (2014), which is used to assign SFR to M_* (see Section 2.3). **Right**: $L_{\rm IR}$–SFR relation based on the IRX–M_* relation from Heinis et al. (2014). The dashed line corresponds to $L_{\rm IR} \propto$ SFR (the Kennicutt relation), which predicts too high $L_{\rm IR}$ for low-mass galaxies (see Section 2.4).

2.3 Star-formation rate from the star-forming main sequence

We assign an SFR to each M_* based on the star-forming main sequence compiled by Speagle et al. (2014):

$$\log_{10}{\rm SFR}(M_*,t) = (0.84{-}0.026{\times}t)\log_{10}M_* - (6.51{-}0.11{\times}t)\ , \quad (1)$$

where t is the age of the universe in Gyr. This relation is shown in the central panel of Figure 1. This compilation is based on the Kroupa IMF, the BC03 SPS model, and the cosmological parameters $\Omega_\Lambda = 0.7$, $\Omega_M = 0.3$, $h = 0.7$. This cosmology is slightly different from our choice; however, these authors stated that the effect of cosmology is negligible for the main sequence calibration.

In our calculation, for each $\log_{10} M_*$, an SFR is drawn from a normal distribution with a mean given by the equation above and a scatter of 0.3 dex. We note that Speagle et al. (2014) have shown that the intrinsic scatter (deconvolved with the evolution in a redshift bin) and the true scatter (excluding observational uncertainties) of the main sequence are 0.3 and 0.2 dex, respectively. We find that a scatter of 0.2 dex produces too low number counts and too low shot noise (see Section 4).

2.4 Infrared luminosity from SFR and stellar mass

To calculate $L_{\rm IR}$, it is commonly assumed that $L_{\rm IR} \propto$ SFR (the Kennicutt relation; Kennicutt 1998; Kennicutt & Evans 2012). However, this relation is known to break down for low mass galaxies, which tend to have lower dust content, lower attenuation, and lower $L_{\rm IR}$ (e.g., Pannella et al. 2009; Garn & Best 2010; Buat et al. 2012; Hayward et al. 2014). One way to improve upon the Kennicutt relation is to assume that the photons produced by star formation are split into UV and IR,

$${\rm SFR} = K_{\rm UV}L_{\rm UV} + K_{\rm IR}L_{\rm IR}\ , \quad (2)$$

and then use a relation between $L_{\rm IR}$ and $L_{\rm UV}$ (e.g., Bernhard et al. 2014). The logarithm of the ratio between $L_{\rm IR}$ and $L_{\rm UV}$ is commonly referred to as the IR-excess (IRX),

$${\rm IRX} = \log_{10}\left(\frac{L_{\rm IR}}{L_{\rm UV}}\right)\ , \quad (3)$$

and has been calibrated observationally. Given the two equations above, we can solve for $L_{\rm IR}$:

$$L_{\rm IR} = \frac{\rm SFR}{K_{\rm IR} + K_{\rm UV}10^{-{\rm IRX}(M_*)}}\ . \quad (4)$$

We use $K_{\rm UV} = 1.71\times10^{-10}$ and $K_{\rm IR} = 1.49\times10^{-10}$ from Kennicutt & Evans (2012) based on the Kroupa IMF .

We adopt the IRX–stellar mass relation from Heinis et al. (2014),

$${\rm IRX}(M_*) = \alpha\log_{10}\left(\frac{M_*}{10^{10.35}{\rm M}_\odot}\right) + {\rm IRX}_0\ , \quad (5)$$

where ${\rm IRX}_0 = 1.32$ and $\alpha = 0.72$. We use $\alpha = 1.5$, which agrees better with the CFIRB amplitudes. Heinis et al. (2014) calibrated the IRX–stellar mass relation based on the rest-frame UV-selected galaxies at $z \sim 1.5$, 3, and 4 in the COSMOS field observed with *Herschel*-SPIRE (part of the HerMES program). Their calibration is down to $M_* \approx 10^{10}{\rm M}_\odot$, and some of their data points at low mass also hint a steeper slope (see their Figure 3).

The right panel of Figure 1 demonstrates the $L_{\rm IR}$–SFR relation from this IRX(M_*), which produces lower $L_{\rm IR}$ for low-SFR galaxies compared with the Kennicutt relation (Kennicutt & Evans 2012, the dashed line). As we will discuss below (Section 4.1), this mass-dependent attenuation is essential for reproducing the observed CFIRB amplitudes.

2.5 Spectral energy distribution

With the $L_{\rm IR}$ calculated above, we need the SED Θ_ν to calculate the spectral flux density S_ν. The spectral luminosity density is given by

$$L_\nu = L_{\rm IR}\Theta_\nu\ , \quad (6)$$

and S_ν at the observed frequency ν is given by

$$S_\nu = \frac{L_{(1+z)\nu}}{4\pi\chi^2(1+z)}\ , \quad (7)$$

where χ is the comoving distance, and $L_{(1+z)\nu}$ is evaluated at the rest-frame frequency $(1+z)\nu$.

We assume that the SED of each galaxy is given by a single-temperature modified blackbody,

$$\Theta_\nu \propto \nu^\beta B_\nu(T_d) \ , \tag{8}$$

where B_ν is the Planck function, T_d is the dust temperature, and β is the spectral index. The SED is normalized such that $\int d\nu \Theta_\nu = 1$. We adopt $\beta = 2.1$ based on our previous work for CFIRB (Wu et al. 2016), and we note that $\beta = 2$ is widely used and theoretically motivated (Draine & Lee 1984; Mathis & Whiffen 1989).

To calculate the T_d of each galaxy, we adopt the relation between T_d and specific star-formation rate (SSFR, SFR/M_*) given by Magnelli et al. (2014),

$$T_d = 98\ [K] \times (1+z)^{-0.065} + 6.9 \log_{10} \mathrm{SSFR} \ , \tag{9}$$

and we assume a normal distribution with a scatter of 2 K around this relation (consistent with their Figure 10). This relation is derived from galaxies up to $z \sim 2$ from the PEP and HerMES programs of *Herschel*. These authors bin galaxies based on SFR, M_*, and z and calculate T_d using the stacked flux density in each bin. They have found that the T_d–SSFR relation is tighter than the T_d–$L_{\rm IR}$ relation.

3 CALCULATING THE CFIRB ANGULAR POWER SPECTRA

With the prediction of S_ν for each halo in the catalogs, we proceed to compute the CFIRB angular power spectra. The formalism presented below is motivated by the analytical halo model presented in Shang et al. (2012), and we make various generalization and adjustments for our sampling approach. Since we use subhaloes from an N-body simulation, we expect our approach to be more accurate than a purely analytical calculation.

The CFIRB auto angular power spectrum is given by the sum of the 2-halo term, the 1-halo term, and the shot noise:

$$C_\ell^\nu = C_\ell^{\nu,\rm 2h} + C_\ell^{\nu,\rm 1h} + C_\ell^{\nu,\rm shot} \ . \tag{10}$$

Here we present the equations for a single frequency; the equations for two-frequency cross-spectra can be generalized easily.

The two-halo term corresponds to the contribution from two galaxies in distinct haloes and is given by

$$C_\ell^{\nu,\rm 2h} = \int \chi^2 d\chi F_\nu^2(z) P_{\rm lin}\left(k = \frac{\ell}{\chi}, z\right) \ , \tag{11}$$

where $P_{\rm lin}(k,z)$ is the linear matter power spectrum calculated with CAMB (Lewis et al. 2000), and

$$F_\nu(z) = \int dM \frac{dn}{dM} b(M) \left(S_\nu^{\rm cen} + \int dM_s \frac{dN(M)}{dM_s} S_\nu^{\rm sat} \right) \ , \tag{12}$$

where M is the mass of central haloes, dn/dM and $b(M)$ are the mass function and halo bias of central haloes, M_s is the mass of subhaloes, and $dN(M)/dM_s$ is the number of subhaloes in a central halo. In our sampling approach, the integration is replaced by the sum over all $b(M)S_\nu$, and for a satellite galaxy we use the $b(M)$ of its central halo. For $b(M)$, we use the fitting function of halo bias from Tinker et al. (2010), and we have verified that this fitting function agrees with the linear halo bias measured directly from the Bolshoi-Planck simulation.

The one-halo term corresponds to the contribution from two galaxies in the same halo and is given by

$$C_\ell^{\nu,\rm 1h} = \int \chi^2 d\chi G_\nu \left(k = \ell/\chi, z\right) \ , \tag{13}$$

where

$$G_\nu(k,z) = 2 \int dM \frac{dn}{dM} S_\nu^{\rm cen} \left(\int dM_s \frac{dN(M)}{dM_s} S_\nu^{\rm sat} \right) u(k,z) + \int dM \frac{dn}{dM} \left(\int dM_s \frac{dN(M)}{dM_s} S_\nu^{\rm sat} \right)^2 u^2(k,z) \ . \tag{14}$$

Here $u(k,z)$ is the density profile of dark matter haloes in the Fourier space, and $u(k,z) \approx 1$ for the large scales discussed in this work. The first term corresponds to summing over the central–satellite pairs in a halo, and the second term corresponds to summing over the satellite–satellite pairs in a halo. We avoid self-pairs in calculating the second term.

The shot noise corresponds to self-pairs of galaxies and is given by

$$C_\ell^{\nu,\rm shot} = \int \chi^2 d\chi \int dS_\nu \frac{dn}{dS_\nu} S_\nu^2 \ , \tag{15}$$

where S_ν includes both central and satellite galaxies.

The cross angular spectrum between CFIRB and CMB lensing potential is given by

$$C_\ell^{\phi\nu} = \int_0^{\chi_*} \chi^2 d\chi (1+z) F_\nu(z) \frac{3}{\ell^2} \Omega_M H_0^2 \left(\frac{\chi_* - \chi}{\chi_* \chi} \right) \times P_{\rm lin}\left(k = \frac{\ell}{\chi}, z\right) \ , \tag{16}$$

where χ_* is the comoving distance to the last-scattering surface, and $F_\nu(z)$ is given by Equation 12.

4 COMPARISON WITH OBSERVATIONS

In this section we compare our model predictions with observational results.

4.1 CFIRB anisotropies

We compare our model with the CFIRB anisotropies observed by *Planck*:

- Planck Collaboration XXX (2014) presents the CFIRB observed by *Planck*-HFI for an area of 2240 deg^2, for which HI maps are available for removing the foreground Galactic dust emission. The primordial CMB, the Sunyaev–Zeldovich effect, and the radio sources are also removed. We compare our model with the CFIRB angular power spectra for $187 \leq \ell \leq 2649$, presented in their Table D.2.
- Planck Collaboration XVIII (2014) presents the first detection of the cross-correlation between CFIRB and CMB lensing potential (the latter is extracted from the low-frequency bands of *Planck*). The CMB lensing potential is dominated by dark matter haloes between $z \approx 1$ and $z \approx 3$, and CFIRB is dominated by galaxies in the same redshift

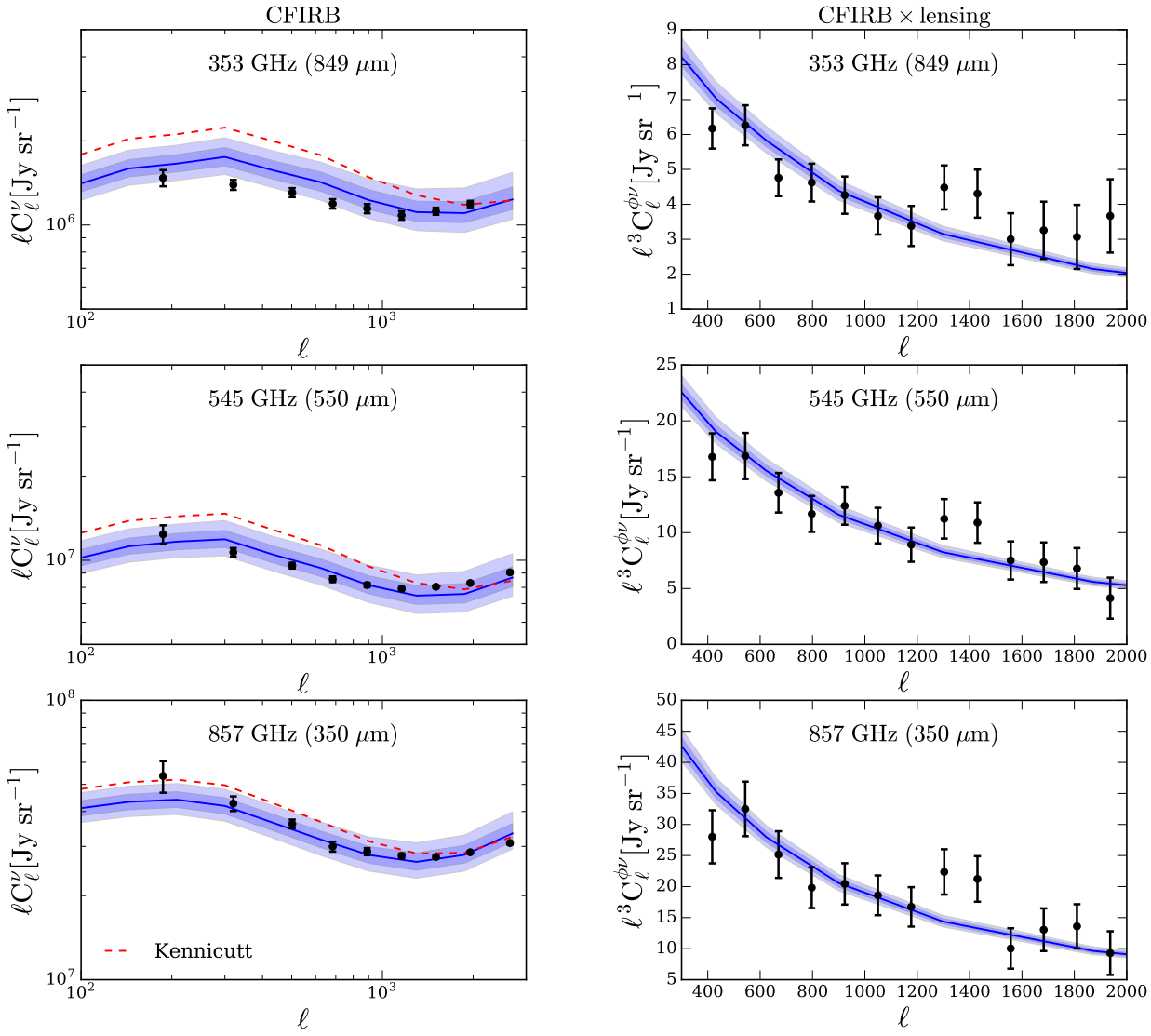

Figure 2. Comparison between our model (blue bands) and the CFIRB anisotropies observed by *Planck* (data points). **Left**: CFIRB auto angular power spectra from Planck Collaboration XXX (2014). The red dashed curves show that the Kennicutt relation over-produces the large-scale amplitudes. **Right**: Cross angular power spectra between CFIRB and CMB lensing potential from Planck Collaboration XVIII (2014). The dark and light blue bands correspond to 68% and 95% intervals of theoretical uncertainties, respectively.

range; therefore, the cross-correlation between CFIRB and CMB lensing potential directly probes the connection between FIR galaxies and dark matter haloes. In addition, compared with the auto-correlation of CFIRB, this cross-correlation is less affected by the contamination of Galactic dust.

Figure 2 compares our model predictions with the observational results described above. We include the results in 353, 545, 857 GHz (849, 550, 350 μm), and we exclude 217 GHz because CMB dominates this band for all angular scales. In all calculations, we apply the color-correction factors and flux cuts of Planck Collaboration XXX (2014, see their Section 5.3 and Table 1). The left column corresponds to the auto angular power spectra of CFIRB, C_ℓ^ν, while the right column corresponds to the cross angular spectra between CFIRB and CMB lensing potential, $C_\ell^{\phi\nu}$. To calculate the theoretical uncertainties, we repeat Steps (iii) to (v) in Section 2 for 1000 times, and we use 0.1% of the haloes in the Bolshoi-Planck simulation to facilitate the calculation. The dark and light blue bands correspond to the 68% and 95% intervals of the theoretical uncertainties. As can be seen, our model well captures both observational results. We emphasize that we perform no fitting to the data, and that all the components of our model directly come from independent surveys of UV, optical, and FIR.

The red dashed curves in the left column of Figure 2 show that, if we assume the Kennicutt relation ($L_{\rm IR} \propto$ SFR) instead of the mass-dependent dust attenuation, we produce too high large-scale amplitudes of the power spectra. The Kennicutt relation assigns too high $L_{\rm IR}$ to low-mass galaxies, and because of the high number density of low-mass

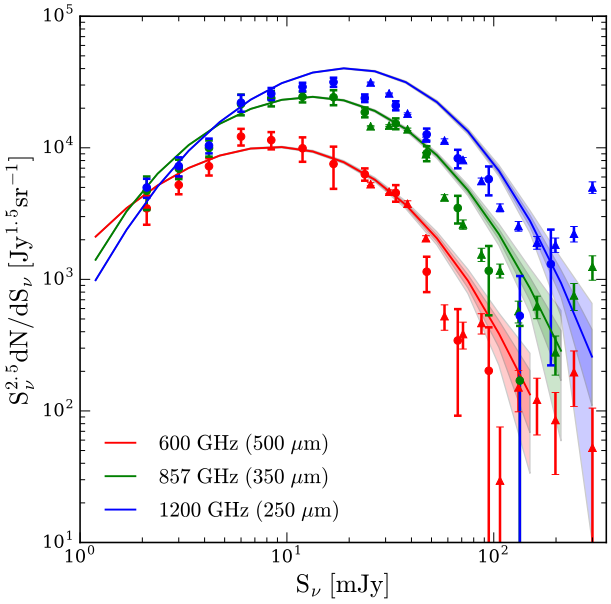

Figure 3. Number counts predicted from our model (color bands) compared with the results from HerMES (Béthermin et al. 2012b, circles) and H-ATLAS (Valiante et al. 2016, triangles). The dark and light bands correspond to 68% and 95% intervals of the theoretical uncertainties, respectively.

galaxies, it leads to too high CFIRB large-scale amplitudes. In this sense, CFIRB can be used to constrain the SFR and dust content of low-mass galaxies. On the other hand, the Kennicutt relation does not affect the small-scale auto-power spectra, which are dominated by shot noise and contributed mostly by massive galaxies.

4.2 Number counts

In this section, we turn to submm number counts, which are dominated by massive galaxies. We compare our model with the number counts observed by *Herschel*-SPIRE at 250, 350, and 500 μm (1200, 857, and 600 GHz):

- Béthermin et al. (2012b) present the deep number counts from the HerMES survey (the COSMOS and GOODS-N fields). They performed stacked analyses based on the 24 μm sources, and they managed to extract the number counts down to ~ 2 mJy.
- Valiante et al. (2016) present the number counts from the H-ATLAS survey of an area of 161.6 deg^2 (the GAMA fields). At the faint end, their results agree with Béthermin et al. (2012b); at the bright end, they have better statistics due to the larger survey area.

Figure 3 compares the number counts from our model with the two observational results described above. For this calculation, we use all halos in the Bolshoi-Planck simulation to obtain enough bright galaxies. We note that the observed brightest end ($\gtrsim 100$ mJy) is dominated by gravitationally lensed sources, which we do not have in our model. Our model mostly agrees with the observational results; however, for 250 μm (1200 GHz) our model produces slightly higher number counts; this could result from our over-simplified assumption for SED.

5 DISCUSSIONS

In our model, we assume that all galaxies belong to the star-forming main sequence. This is a simplified assumption, because it is known that a fraction of massive galaxies are quiescent (e.g., Ilbert et al. 2013; Moustakas et al. 2013; Muzzin et al. 2013; Tomczak et al. 2014; Schreiber et al. 2016; Man et al. 2016). However, studies have also shown that quiescent galaxies can still have significant FIR emission due to the dust heated by old stars (the so-called cirrus dust emission, e.g., Fumagalli et al. 2014; Hayward et al. 2014; Narayanan et al. 2015). In Wu et al. (2016), we have also found that the observed CFIRB requires substantial FIR emission from massive haloes, which are usually expected to host quiescent galaxies. Therefore, quiescent galaxies can still contribute significantly to CFIRB, and the quiescent fraction and the cirrus dust emission are degenerate. Investigating this degeneracy will require the modeling of old stars and cirrus dust, as well as comparisons with near-infrared observations. We will investigate this in future work.

On the other hand, it is also known that a small fraction of galaxies undergo starburst phases and have significantly higher SFR and IR luminosities (e.g., Elbaz et al. 2011). The starburst galaxies account for $\sim 10\%$ of the cosmic SFR density at $z \sim 2$ (Rodighiero et al. 2011; Sargent et al. 2012) and are expected to have negligible contribution to the CFIRB (e.g., Shang et al. 2012; Béthermin et al. 2013). The effect of starburst galaxies will be degenerate with that of quiescent galaxies in producing CFIRB. Therefore, any departure from the star-forming main sequence will require constraints from multi-wavelength observations, which will be explored in our future work.

In this work, we choose a minimal number of modeling steps in order to avoid degeneracies. Except for the slope of the IRX–M_* relation, all the other parameter values are directly taken from the literature, and we neither introduce new parameters nor fit parameters to the data. In our future work, we plan to include more astrophysical processes (including quiescent and starburst galaxies, more realistic SEDs) into our model and perform Markov chain Monte Carlo calculations to constrain model parameters, combining multi-wavelength observational results from UV, optical, near-IR, FIR, and radio surveys.

Over the next decade, new instruments are expected to revolutionize the view of the FIR/submm sky. The Far-infrared Surveyor (Origins Space Telescope), which is currently planned by NASA, prioritizes the measurements of cosmic star-formation rate. In addition, the next generation CMB S4 ground-based telescopes (Abazajian et al. 2016) will measure CMB lensing and CFIRB to unprecedented precision, enabling more detailed studies of cross-correlation. The Primordial Inflation Explorer (PIXIE, Kogut et al. 2011) will significantly improve the accuracy of the absolute intensity of CFIRB compared with *COBE*-FIRAS. These missions are expected to lead to a consistent picture of cosmic star-formation history. We plan to apply the empirical approach presented in this paper to generate mock catalogs, check consistencies between models, and develop survey strategies for these observational programs.

6 SUMMARY

We present a minimal empirical model for dusty star-forming galaxies to interpret the observations of CFIRB anisotropies and submm number counts. Our model is based on the Bolshoi-Planck simulation and various results from UV/optical/IR galaxy surveys. Below we summarize our model and findings:

- To assign IR spectral flux densities S_ν to dark matter haloes, we model stellar mass (using abundance matching between $v_{\rm peak}$ and observed stellar mass functions), SFR (using the star-forming main sequence), $L_{\rm IR}$ (assuming a mass-dependent attenuation), and SED (assuming a modified blackbody).
- Given the connection between S_ν and halo mass obtained above, we apply an extended halo model to calculate the auto angular power spectra of CFIRB and the cross angular power spectra between CFIRB and CMB lensing potential. Our model produces power spectra that agree well with those observed by *Planck*.
- A steep mass-dependent dust attenuation is necessary for reproducing the amplitudes of the observed CFIRB power spectra. The commonly used Kennicutt relation, $L_{\rm IR} \propto$ SFR, leads to too high $L_{\rm IR}$ for low-mass galaxies and thus too high CFIRB amplitudes.
- Our model also produces submm number counts that agree with observational results of *Herschel*. The number counts are contributed by massive haloes, and this agreement indicates that our minimal model (star-forming main sequence only, no quiescent or starburst galaxies) is sufficient for dusty star-forming galaxies in massive haloes. We slightly over-produce the number counts at 250 μm (1200 GHz), and this may indicate that the SEDs of dust emission deviate from a simple modified blackbody.

Our results indicate that the observed CFIRB broadly agrees with the current knowledge of galaxy evolution from resolved galaxies in UV and optical surveys, under the assumption that low-mass galaxies produces IR luminosities lower than expected from the Kennicutt relation. Therefore, CFIRB provides a rare opportunity of constraining the SFR and dust production in low-mass galaxies. However, since CFIRB does not provide redshifts of galaxies, further investigations for low-mass galaxies will require the cross-correlation between CFIRB with galaxies or background light observed in other wavelengths (e.g., Cooray 2016; Serra et al. 2016).

ACKNOWLEDGEMENTS

We thank Joanne Cohn and Martin White for helpful discussions, and we thank Yao-Yuan Mao for providing the code and assistance for the abundance matching calculation. H.W. acknowledges the support by the U.S. National Science Foundation (NSF) grant AST1313037. The calculations in this work were performed on the Caltech computer cluster Zwicky, which is supported by NSF MRI-R2 award number PHY-096029. Part of the research described in this paper was carried out at the Jet Propulsion Laboratory, California Institute of Technology, under a contract with the National Aeronautics and Space Administration.

REFERENCES

Abazajian K. N., et al., 2016, preprint, (arXiv:1610.02743)
Addison G. E., Dunkley J., Bond J. R., 2013, MNRAS, 436, 1896
Amblard A., Cooray A., Serra P., et al., 2011, Nature, 470, 510
Behroozi P. S., Conroy C., Wechsler R. H., 2010, ApJ, 717, 379
Behroozi P. S., Wechsler R. H., Wu H.-Y., 2013a, ApJ, 762, 109
Behroozi P. S., Wechsler R. H., Wu H.-Y., Busha M. T., Klypin A. A., Primack J. R., 2013b, ApJ, 763, 18
Behroozi P. S., Wechsler R. H., Conroy C., 2013c, ApJ, 770, 57
Bernhard E., Béthermin M., Sargent M., Buat V., Mullaney J. R., Pannella M., Heinis S., Daddi E., 2014, MNRAS, 442, 509
Berta S., Magnelli B., Nordon R., et al., 2011, A&A, 532, A49
Béthermin M., Doré O., Lagache G., 2012a, A&A, 537, L5
Béthermin M., Le Floc'h E., Ilbert O., et al., 2012b, A&A, 542, A58
Béthermin M., et al., 2012c, ApJ, 757, L23
Béthermin M., Wang L., Doré O., Lagache G., Sargent M., Daddi E., Cousin M., Aussel H., 2013, A&A, 557, A66
Bruzual G., Charlot S., 2003, MNRAS, 344, 1000
Buat V., et al., 2012, A&A, 545, A141
Casey C. M., Narayanan D., Cooray A., 2014, Phys. Rep., 541, 45
Conroy C., Wechsler R. H., Kravtsov A. V., 2006, ApJ, 647, 201
Cooray A., 2016, Royal Society Open Science, 3, 150555
De Bernardis F., Cooray A., 2012, ApJ, 760, 14
Draine B. T., Lee H. M., 1984, ApJ, 285, 89
Dunlop J. S., et al., 2016, preprint, (arXiv:1606.00227)
Elbaz D., et al., 2011, A&A, 533, A119
Fixsen D. J., Dwek E., Mather J. C., Bennett C. L., Shafer R. A., 1998, ApJ, 508, 123
Fujimoto S., Ouchi M., Ono Y., Shibuya T., Ishigaki M., Nagai H., Momose R., 2016, ApJS, 222, 1
Fumagalli M., Labbé I., Patel S. G., et al., 2014, ApJ, 796, 35
Garn T., Best P. N., 2010, MNRAS, 409, 421
Geach J. E., Dunlop J. S., Halpern M., et al., 2016, preprint, (arXiv:1607.03904)
Gispert R., Lagache G., Puget J. L., 2000, A&A, 360, 1
Hajian A., Viero M. P., Addison G., et al., 2012, ApJ, 744, 40
Hall N. R., Keisler R., Knox L., et al., 2010, ApJ, 718, 632
Hauser M. G., Dwek E., 2001, ARA&A, 39, 249
Hauser M. G., Arendt R. G., Kelsall T., et al., 1998, ApJ, 508, 25
Hayward C. C., et al., 2014, MNRAS, 445, 1598
Heinis S., Buat V., Béthermin M., et al., 2014, MNRAS, 437, 1268
Henriques B. M. B., White S. D. M., Thomas P. A., Angulo R., Guo Q., Lemson G., Springel V., Overzier R., 2015, MNRAS, 451, 2663
Ilbert O., et al., 2013, A&A, 556, A55
Kennicutt Jr. R. C., 1998, ApJ, 498, 541
Kennicutt R. C., Evans N. J., 2012, ARA&A, 50, 531
Kogut A., et al., 2011, J. Cosmol. Astropart. Phys., 7, 25
Kroupa P., 2001, MNRAS, 322, 231
Lagache G., Bavouzet N., Fernandez-Conde N., Ponthieu N., Rodet T., Dole H., Miville-Deschênes M.-A., Puget J.-L., 2007, ApJ, 665, L89
Lewis A., Challinor A., Lasenby A., 2000, ApJ, 538, 473
Lutz D., 2014, ARA&A, 52, 373
Madau P., Dickinson M., 2014, ARA&A, 52, 415
Magnelli B., Lutz D., Saintonge A., et al., 2014, A&A, 561, A86
Man A. W. S., et al., 2016, ApJ, 820, 11
Mathis J. S., Whiffen G., 1989, ApJ, 341, 808
Matsuura S., et al., 2011, ApJ, 737, 2
Moster B. P., Naab T., White S. D. M., 2013, MNRAS, 428, 3121
Moustakas J., et al., 2013, ApJ, 767, 50
Muzzin A., et al., 2013, ApJ, 777, 18
Nagai D., Kravtsov A. V., 2005, ApJ, 618, 557

Narayanan D., Turk M., Feldmann R., et al., 2015, Nature, 525, 496
Pannella M., et al., 2009, ApJ, 698, L116
Partridge R. B., Peebles P. J. E., 1967, ApJ, 148, 377
Planck Collaboration XVI 2014, A&A, 571, A16
Planck Collaboration XVIII 2011, A&A, 536, A18
Planck Collaboration XVIII 2014, A&A, 571, A18
Planck Collaboration XXX 2014, A&A, 571, A30
Puget J.-L., Abergel A., Bernard J.-P., Boulanger F., Burton W. B., Desert F.-X., Hartmann D., 1996, A&A, 308, L5
Reddick R. M., Wechsler R. H., Tinker J. L., Behroozi P. S., 2013, ApJ, 771, 30
Rodighiero G., et al., 2011, ApJ, 739, L40
Rodríguez-Puebla A., Behroozi P., Primack J., Klypin A., Lee C., Hellinger D., 2016, MNRAS, 462, 893
Sargent M. T., Béthermin M., Daddi E., Elbaz D., 2012, ApJ, 747, L31
Schreiber C., Elbaz D., Pannella M., Ciesla L., Wang T., Koekemoer A., Rafelski M., Daddi E., 2016, A&A, 589, A35
Serra P., Doré O., Lagache G., 2016, preprint, (arXiv:1608.00585)
Shang C., Haiman Z., Knox L., Oh S. P., 2012, MNRAS, 421, 2832
Shankar F., Lapi A., Salucci P., De Zotti G., Danese L., 2006, ApJ, 643, 14
Song M., et al., 2016, ApJ, 825, 5
Speagle J. S., Steinhardt C. L., Capak P. L., Silverman J. D., 2014, ApJS, 214, 15
Thacker C., Gong Y., Cooray A., De Bernardis F., Smidt J., Mitchell-Wynne K., 2015, ApJ, 811, 125
Tinker J. L., Robertson B. E., Kravtsov A. V., Klypin A., Warren M. S., Yepes G., Gottlöber S., 2010, ApJ, 724, 878
Tomczak A. R., et al., 2014, ApJ, 783, 85
Vale A., Ostriker J. P., 2004, MNRAS, 353, 189
Valiante E., et al., 2016, MNRAS, 462, 3146
Viero M. P., Ade P. A. R., Bock J. J., et al., 2009, ApJ, 707, 1766
Viero M. P., Wang L., Zemcov M., et al., 2013, ApJ, 772, 77
Wang L., Li C., Kauffmann G., De Lucia G., 2006, MNRAS, 371, 537
Wetzel A. R., White M., 2010, MNRAS, 403, 1072
Wu H.-Y., Doré O., Teyssier R., 2016, preprint, (arXiv:1607.02546)
Xia J.-Q., Negrello M., Lapi A., De Zotti G., Danese L., Viel M., 2012, MNRAS, 422, 1324

APPENDIX A: FITTING THE OBSERVED STELLAR MASS FUNCTIONS

In Section 2.2, we fit redshift-dependent Schechter functions to the observed stellar mass functions. We minimize

$$\chi^2 = \frac{\sum(\log_{10}\Phi_{\rm model} - \log_{10}\Phi_{\rm data})^2}{(\Delta\log_{10}\Phi_{\rm data})^2} \ . \tag{A1}$$

For $0 \le z \le 3.5$, we use a double Schechter function:

$$\begin{aligned}\Phi(M_*) &= \frac{dn}{d\log_{10}M_*}[{\rm Mpc}^{-3}{\rm dex}^{-1}] \\ &= (\Phi_1 m^{1+\alpha_1} + \Phi_2 m^{1+\alpha_2})e^{-m}\ln(10) \ ,\end{aligned} \tag{A2}$$

where

$$m = \frac{M_*}{M_0} \ . \tag{A3}$$

We assume that M_0, Φ_1, and Φ_2 depend on z, while α_1 and α_2 are independent of z. The best-fit parameters are

$$\begin{aligned}\log_{10}M_0 &= 10.90 + 0.08\times z \\ \log_{10}\Phi_1 &= -2.4 - 0.61\times z \\ \log_{10}\Phi_2 &= -3.29 - 0.23\times z \\ \alpha_1 &= -0.68 \\ \alpha_2 &= -1.57\end{aligned} \tag{A4}$$

with $\chi^2 = 7.4$ with 41 degrees of freedom.

For $3.5 < z \le 6$, we use a single Schechter function:

$$\Phi(M_*) = \Phi_1 m^{1+\alpha_1} e^{-m}\ln(10) \ , \tag{A5}$$

and we assume that all parameters depend on $\ln(1+z)$. The best-fit parameters are

$$\begin{aligned}\log_{10}M_0 &= 12.26 - 0.77\times\ln(1+z) \\ \log_{10}\Phi_1 &= -0.77 - 1.99\times\ln(1+z) \\ \alpha_1 &= -0.47 - 0.69\times\ln(1+z)\end{aligned} \tag{A6}$$

with $\chi^2 = 3.7$ with 19 degrees of freedom. The fitting functions are shown in the left panel of Figure 1.

This paper has been typeset from a TEX/LATEX file prepared by the author.